analytical chemistry

Article

pubs.acs.org/ac

Electrical Detection Method for Circulating Tumor Cells Using Graphene Nanoplates

Song-I Han and Ki-Ho Han*

Department of Nano Science and Engineering, Center for Nano Manufacturing, Inje University, 607 Obang-dong, Gimhae, Gyongnam 621-749, Republic of Korea

Supporting Information

ABSTRACT: This paper presents a microfluidic device for electrical discrimination of circulating tumor cells (CTCs) using graphene nanoplates (GNPs) as a highly conductive material bound to the cell surface. For two-step cascade discrimination, the microfluidic device is composed of a CTC-enrichment device and an impedance cytometry. Using lateral magnetophoresis, the CTC-enrichment device enriches rare CTCs from millions of background blood cells. Then, the impedance cytometry electrically identifies CTCs from the enriched sample, containing CTCs and persistent residual blood cells, based on the electrical impedance of CTCs modified by the GNPs. GNPs were used as a highly conductive material for modifying surface conductivity of CTCs, thereby improving the accuracy of electrical discrimination. The experimental results showed that a colorectal cancer cell line (DLD-1) spiked into peripheral blood was enriched by nearly 500-fold by the CTC-enrichment device. The phase of the electrical signal measured from DLD-1 cells covered by GNPs shifted by about 100° in comparison with that from normal blood cells, which allows the impedance cytometry to identify CTCs at a rate of 94% from the enriched samples.

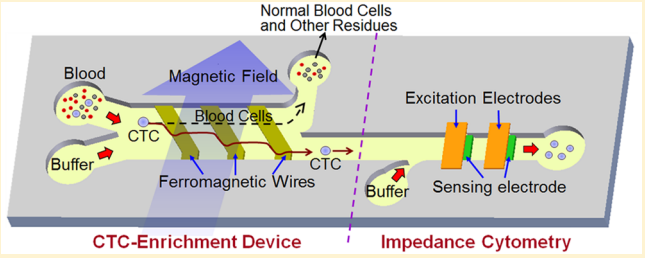

Primary tumors release cancer cells into the bloodstream, resulting in the occurrence of so-called circulating tumor cells (CTCs). Many recent studies have shown that the number of CTCs in peripheral blood can be useful for early diagnosis of cancer, predicting disease progression and suggesting therapeutic interventions.[1−4] However, it is very difficult to find CTCs in blood because their population is extremely small, ranging from 1 to 200 cells per milliliter of blood.[5,6]

Several methods for isolation of CTCs from peripheral blood have been reported previously, including filtration based on size and deformability,[7−13] density gradient,[14,15] immunomagnetic beads,[16−18] microposts,[19−21] microfluidic mixing structures,[22] laminar vortices,[23] spiral microchannels,[24] and dielectric properties.[25,26] The most common method for isolating CTCs is magnetic-activated cell sorting (MACS) based on immunomagnetic beads because this has the advantage of high accuracy and can be carried out using a simple system. CellSearch (Janssen Diagnostics, LLC) is a commercial product for enrichment and discrimination of CTCs based on the MACS method. However, due to its limited performance for low-purity enriched samples containing CTCs and residual blood cells, the discrimination process using fluorescence images requires a prolonged time and also has a high risk of error.

Flow cytometry can obtain information for cell identification in real-time when passing through the detection spot, thereby rapidly and accurately detecting target cells from heterogeneous cell mixtures. Flow cytometry can be classified into two systems depending on the detection mechanism using light or electrical signals. Fluorescence-activated cell sorting (FACS), which is a type of flow cytometry using light signals, can enumerate and quantify CTCs from peripheral blood by immunofluorescence staining.[27,28] However, as FACS requires a number of target cells in the starting sample, it is not appropriate for directly detecting CTCs from whole blood due to their rarity.

The Coulter counter is a representative flow cytometer using electrical signals. As the amplitude of the electrical signal is proportional to the volume of cell, the amplitude can be used as a criterion for discrimination of CTCs because they are commonly larger than normal blood cells. As the criterion is based only on cell size, it can be limited for application to detect CTCs, which have various sizes.[29−31] Therefore, electrical cytometry in a microfluidic device format[32] was developed for discriminating CTCs using multiple criteria, such as the magnitude, shape, and transit time of the electrical signal. However, it was not appropriate for detecting rare cells from a heterogeneous cell mixture as a starting sample. To improve the performance, electrical and fluorescence detection methods were combined, thereby leading to more informative systems.[33−35] Even though the fluorescence detection method is the most common and precise approach to detect cells, the system is still bulky and complicated with light sources and other optical components.

Received: August 6, 2015
Accepted: September 24, 2015
Published: September 24, 2015

DOI: 10.1021/acs.analchem.5b03147
Anal. Chem. 2015, 87, 10585−10592

In this paper, we introduce a microfluidic device (the CTC-eChip) for discriminating CTCs based on two electrical parameters, i.e., amplitude and phase difference of the sensing signal. As a tandem platform, the CTC-eChip is composed of a CTC-enrichment device and an impedance cytometry. To improve the isolation accuracy, the CTC-enrichment device is first used for enrichment of CTCs from blood, based on immunomagnetic nanobeads (MNBs) and the lateral magnetophoresis method. Then, the enriched CTCs are sequentially identified by impedance cytometry, based on the signal amplitude determined by cell size and the phase difference changed by the electrical properties of CTCs modified by graphene nanoplates (GNPs) as a highly conductive material bound to the cell surface. An amplitude modulation sensing method was developed to reduce electrical noise, thereby obtaining a sensitive output signal with a high signal-to-noise ratio. To verify the feasibility of the proposed electrical detection method for CTCs, the colorectal cancer cell line DLD-1 was spiked into peripheral blood, enriched by the CTC-enrichment device, and identified by impedance cytometry. The numbers of enriched and identified DLD-1 cells were compared by regression analysis.

MATERIALS AND METHODS

Detailed fabrication process, experimental setup, and sample preparation are explained in Supporting Information S1.

Design and Working Principle. To achieve the two-step cascade discrimination of the CTC-eChip, CTCs spiked into whole blood were first labeled with MNBs and GNPs using an antiepithelial cell adhesion molecule (EpCAM), a common surface marker of epithelial-derived carcinoma cells, as shown in Figure S1. The CTC-enrichment device can then enrich CTCs labeled by MNBs based on lateral magnetophoresis, and impedance cytometry can electrically identify CTCs covered by GNPs.

The CTC-enrichment device consists of two inlets, two outlets, and a ferromagnetic permalloy wire array inlaid in the bottom substrate, as shown in Figure 1A. A blood sample and 0.1% BSA in PBS are injected at the same flow rate through the sample and buffer inlets, respectively. For the flow rate of the impedance cytometry, channel widths of outlets no. 1 and no. 2 were 100 and 900 μm, respectively. To allow for a stronger magnetic force (F_m) than the hydrodynamic drag force (F_d sin θ) in the lateral direction,[16,36] the ferromagnetic wire array was placed at an angle of θ (=5.7°) to the direction of flow. Due to the SU-8 lithography process, the thickness of the ferromagnetic wires was limited to 40 μm. To prevent saturation of the magnetic force,[37] the width of the wires was designed to be 50 μm with an interval of 300 μm. To reduce aggregation and stacking of CTCs at corners comprised of the ferromagnetic wires and the sidewall of the microchannel, one end of the ferromagnetic wires was bent at almost a right angle 50 μm before reaching the sidewall, thereby placing the bent parts of the wires parallel with the direction of the external magnetic field, as shown in Figure 1A.

When a uniform external magnetic field is applied to the ferromagnetic wire, a high-gradient magnetic field is generated at the edge of the inlaid ferromagnetic wire (Figure 1B).[38] CTCs labeled with MNBs experience magnetic force and hydrodynamic drag force at the same time as passing over the wire. Therefore, the lateral magnetic force (F_l)[37] acting on CTCs is generated as the vector sum of the magnetic force and the drag force. Then, CTCs move laterally along the edge of the wire and flow into outlet no. 1, which is connected to the inlet of the impedance cytometry. Meanwhile, normal blood cells and debris are discarded via outlet no. 2.

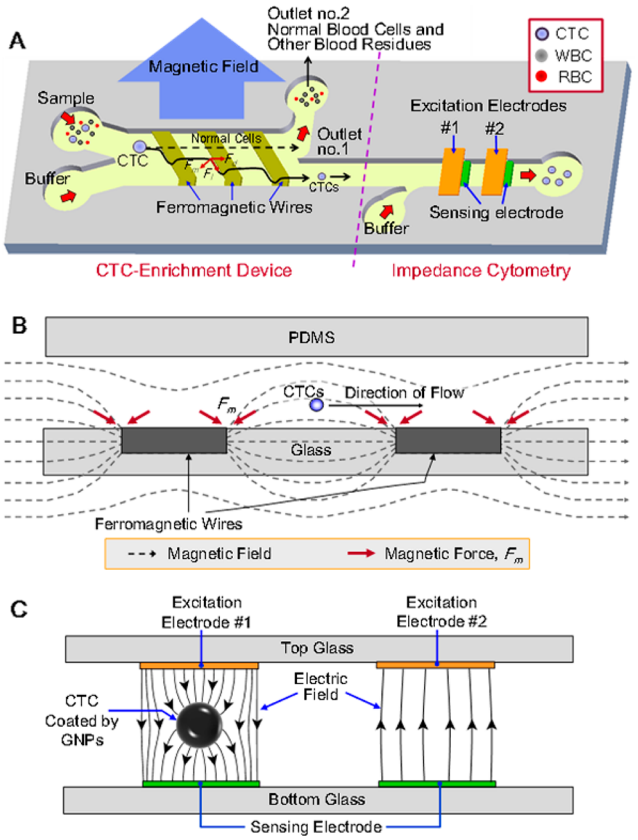

Figure 1. (A) Perspective view of the CTC-eChip composed of the CTC-enrichment device and impedance cytometry. On the basis of lateral magnetophoresis, CTCs are first enriched from blood by the CTC-enrichment device and subsequently identified by impedance cytometry. (B) Cross-sectional view of the inlaid ferromagnetic wire array with the gradient magnetic field in the microchannel. CTCs bound to MNBs are laterally separated along with the edge of the ferromagnetic wires by the magnetic force (F_m) and the drag force (F_d). (C) Schematic view of the electric field distribution between the excitation and sensing electrode pairs with a CTC covered with GNPs (left) and without (right). Electrical fields tend to flow through GNPs, because their conductivity is higher than the medium value.

The impedance cytometry consists of two inlets, one outlet, and an electrical sensing region. Sample and buffer inlets are used to inject cells enriched by the CTC-enrichment device and buffer solution consisting of PBS with 0.1% BSA, respectively. To avoid sedimentation of CTCs, the buffer solution is used to push the cells. Two excitation electrodes and two sensing electrodes, patterned on the top and bottom of the microchannel, are aligned in parallel to optimize the detection sensitivity, as shown in Figure 1A. In addition, to increase CTC detection accuracy, both the amplitude and phase of the sensing signal, produced by their size and electrical properties, are used as discrimination criteria. To reduce ensemble noise, an excitation voltage with superposition of two sinusoidal signals of 500 kHz and 10 MHz is applied to the two excitation electrodes out of phase with one another. When a CTC passes through one of the excitation and sensing electrode pairs, the imbalance between the two electrode pairs induces an amplitude-modulated signal on the sensing electrode. Then, the amplitude at 500 kHz and the phase at 10 MHz can be

DOI: 10.1021/acs.analchem.5b03147
Anal. Chem. 2015, 87, 10585−10592

obtained by demodulation of the sensing signal. As CTCs are generally larger than normal blood cells, the amplitude is one criterion for identifying these abnormal cells.[39] When a CTC covered by GNPs passes through one of the electrode pairs, the resistance of the electrode pair will be lower than that of the other electrode filled with medium because electrical current flows mainly through GNPs, which have higher conductivity than medium (Figure 1C). In contrast, when a normal cell passes through the electrodes, the resistance increases because conductivity of cytoplasm is normally lower than that of the medium. Consequently, GNPs on the surface of CTCs generate a phase difference comparison in normal cells, which can be used a discrimination criterion along with the amplitude. Finally, to verify the possibility of downstream analysis, the RT-PCR process using discriminated DLD-1 cells was performed and the process was described in more detail in Supporting Information S2.

Theory. When a CTC covered by GNPs is placed between the excitation and sensing electrodes, the electrodes pair can be modeled by an equivalent circuit, as shown in Figure S6. As the geometrical factors of the detection system, such as size of electrodes and the sensing dimensions, are decided by the design and fabrication process, the parameters R_m, R'_m, C_m, C'_m, and C_{mem} of the equivalent circuit can be calculated by the conductivities and permittivities of the cell and the suspending medium[40] obtained using Maxwell's mixture theory.[41−43]

In the case of bare CTCs, the equivalent circuit parameters of CTCs are composed of the membrane capacitance C_{mem}, the resistance of the cytoplasm R_i, and the resistance of the suspending medium R''_m. The cell resistance is divided into R_i and R''_m depending on the different conductivities, which can be expressed as follows:

$$R_i = \frac{4}{9\Phi l\alpha}\left(\frac{1}{\sigma_i}\right) \tag{1}$$

$$R''_m = \frac{4}{9\Phi l\alpha}\left(\frac{1}{2\sigma_m}\right) \tag{2}$$

with

$$\Phi = \frac{4}{3}\pi r^3 \frac{1}{whl} \tag{3}$$

$$\alpha = \frac{1}{\pi}\ln\left(4\frac{1+\beta^{1/2}}{1-\beta^{1/2}}\right) \tag{4}$$

$$\beta = \tanh\left(\frac{\pi w}{2h}\right) \tag{5}$$

where σ_i and σ_m are the conductivities of the cytoplasm and suspending medium, respectively. Φ is the volume fraction of a cell to the detection volume. h (=25 μm) and w (=20 μm) are the height and width of the microchannel, respectively, and l (=30 μm) is the electrode length. α is the geometrical cell constant for the impedance-sensing region, solved using the Schwarz−Christoffel mapping method that takes into account the nonuniform electric field.[44]

The equivalent circuit model of CTC covered by GNPs includes the resistance and capacitance of GNP, R_G and C_G, respectively, expressed as follows:

$$R_G = \left(\frac{r}{d}\right)\frac{4}{9\Phi l\alpha}\left(\frac{1}{\sigma_G}\right) \tag{6}$$

$$C_G = \frac{9\Phi r C_{G,dl}}{4} l\alpha \tag{7}$$

where σ_G is the conductivity of GNP. The resistance of GNP R_G contains a factor of the membrane layer, which is the ratio of the thickness (d = 50 nm) of GNP and the radius (r) of CTC. $C_{G,dl}$ is a double layer capacitance between GNP and medium and can be considered a specific membrane capacitance connected to C_{mem} in parallel.[45−47]

RESULTS AND DISCUSSION

GNP Coverage Rate. The number of GNPs added per cell in the sample should be optimized to reduce the formation of free GNPs and increase the coverage rate of GNPs on the cells. For example, the optimal number of microbeads (radius: 0.5−5 μm) per cell is typically 100−10 000.[48] As the number of nucleated cells in 100 μL of blood is approximately 5×10^5, we used 10^8 GNPs for preparation of the blood samples. The coverage rate of GNPs is also proportional to the expression level of the targeted membrane antibody of DLD-1 cells.[49] As EpCAM is highly expressed on DLD-1 cells,[50] binding of GNPs targeting EpCAM can increase the coverage rate of GNPs, thereby increasing the phase shift of DLD-1 cells covered by GNPs. Figure 2A,B shows white light illumination and fluorescence images of a DLD-1 cell covered by GNPs.

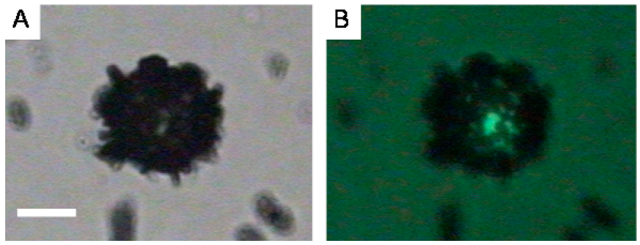

Figure 2. (A) White light illumination image and (B) fluorescence image of a DLD-1 cell covered by GNPs. White scale bar is 10 μm.

As the GNP coverage rate, x, on DLD-1 cells increases, current flowing through GNPs on DLD-1 cells will also increase. Then, the effective resistance, R_{eff}, of DLD-1 cells covered by GNPs becomes the parallel resistance of R_i and R_G/x and the effective capacitance, C_{eff}, is the parallel capacitance of C_{mem} and xC_G, as shown in Figure S7. These can be expressed as follows:

$$R_{eff} = \frac{R_G R_i}{R_G + xR_i} \tag{8}$$

$$C_{eff} = xC_G + C_{mem} \tag{9}$$

where R_{eff} and C_{eff} values for varying x from 0 to 1 are calculated in Table 1. When DLD-1 cells are not covered by GNPs, x = 0, R_{eff} is the same as the resistance of the DLD-1 cytoplasm R_i, and C_{eff} is C_{mem}. However, when the DLD-1 cell is completely covered by GNPs, x = 1, the conductivity of GNP σ_G and the double layer capacitance between GNP and the surrounding medium $C_{G,dl}$ are used to calculate the equivalent circuit parameters, R_G and C_G. The effective resistance is

DOI: 10.1021/acs.analchem.5b03147
Anal. Chem. 2015, 87, 10585−10592

Table 1. Equivalent Circuit Parameters of DLD-1 Cells Covered by GNPs According to the Coverage Rate, *x*, of GNPs

x GNP coverage rate of DLD-1	R_{eff} (kΩ)	C_{eff} (pF)
0	71.39	1.02
0.02	63.11	1.17
0.04	56.56	1.32
0.08	46.83	1.61
0.2	30.89	2.49
1	9.45	8.38

steadily decreased and the effective capacitance is increased with the GNP coverage rate.

The amplitude and phase spectra of DLD-1 cells covered by GNPs could be theoretically simulated using R_{eff} and C_{eff} for varying coverage rate, *x*, of GNPs, as shown in Figure S8A,B. Peaks of amplitude are mostly placed around 500 kHz. As C_{eff} increases with the coverage rate of GNPs, in the case of $x = 1$, the frequency of the plateau is shifted toward the high frequency side. Meanwhile, the amplitude and phase difference at high frequency consistently increase with the coverage rate of GNPs, because the impedance, $1/(2\pi f C_{eff})$, of the effective capacitance in Figure S7 is inversely proportional to the frequency, *f*.

Impedance Spectra of Bare DLD-1 and DLD-1 Covered by GNPs, WBC, and GNP Clot. The simulated and measured amplitude and phase spectra of bare DLD-1 cells, DLD-1 cells covered by GNPs, WBCs, and GNP clot are shown in Figure 3A,B. The equivalent circuit parameters, summarized in Table S1, were calculated using the dielectric properties[51,52] of bare DLD-1 cells, DLD-1 cells covered by GNPs, WBCs, and GNP clot. The radii of DLD-1 cells and WBCs were measured as 7.19 and 4.14 μm, respectively, using a Coulter counter (Z2, Beckman Coulter). The GNP clot radius was estimated as about 2.5 μm from the amplitude spectrum. For fitting the simulation results to the measured data, both the cytoplasm conductivities, σ_i, of DLD-1 cells and WBCs were calculated as 1.3 S m^{-1}, which was consistent with previously reported values.[52−55] The area-specific membrane capacitance of GNP, $C_{G,dl}$, of 100 mF m^{-2}, was calculated from the equation of double layer capacitance[44] and was about 7-fold higher than the area-specific membrane capacitance of normal cells, $C_{mem,0}$, of 13.9 mF m^{-2}, under the assumption that the cell membrane thickness is 5 nm. The measured data of DLD-1 cells covered by GNPs in Figure 3A,B could be compared with the simulation results of DLD-1, 8% covered by GNPs in Figure S8A,B. The double layer capacitance C_{dl} measured by an impedance analyzer (HP4194A, Agilent) and analyzed using the constant phase element (CPE) and RC model was 50 pF, presented in Supporting Information S3. While the parasitic capacitance C_p was obtained as 0.2 pF from the fitted data in Figure S12, the parasitic capacitance from the fitted data in Figure 3A,B was 2 pF, due to the other parasitic capacitance of the signal processing circuitry. Due to the electrical properties between the excitation and sensing electrodes, the electrical impedance was measured in a limited frequency range from 100 kHz to 10 MHz.

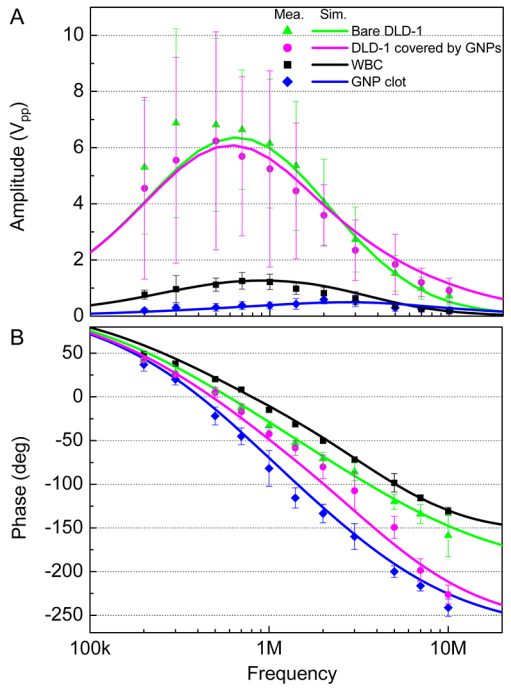

Figure 3. Comparison of the simulated and measured results of the (A) amplitude and (B) phase spectra of bare DLD-1 cells, DLD-1 cells covered by GNPs, WBCs, and GNP clot. The points are mean values of 1000 measured data sets, and the error bars represent the first standard deviation. The solid lines are the PSPICE simulation results using the equivalent circuit model in Figure S6.

As shown in Figure 3A, the amplitudes of bare DLD-1 cells, DLD-1 cells covered by GNPs, and WBCs were maximum at about 500 kHz and decreased markedly by interfacial relaxation of the cell membrane at frequencies higher than 1 MHz. The amplitude variation at low frequency was larger than that at high frequency, which means that the detection sensitivity at low frequency was higher than that at high frequency. The amplitude of DLD-1 covered by GNPs did not significant differ with that of bare DLD-1 in the frequency range of 0.1−10 MHz. Therefore, to minimize the effects of the double layer and cell membrane capacitances, the amplitude measured at 500 kHz was used as a criterion for discriminating the DLD-1 cell and WBC. Figure 3B shows that the phase of DLD-1 cells covered by GNPs and the GNP clot were certainly different from the phase of bare DLD-1 cells and WBCs and the phase difference increased up to about 100° as the frequency increased. In this study, to obtain a significant phase difference, measurements were performed at 10 MHz.

Amplitude Criterion. To determine the amplitude criterion for discriminating DLD-1 cells and WBCs based on their size, the volume histogram of DLD-1 cells and WBCs was measured using a Coulter counter (Figure S9A) and compared with the amplitude histogram measured by impedance cytometry (Figure S9B). As the amplitude of the output signal of impedance cytometry is linearly proportional to the volume of the cell, the volume and amplitude histograms can be compared with each other. The volume histogram shows that the average volume of WBCs is 295.9 μm^3, the majority of WBCs are smaller than 600 μm^3, and residual RBCs and debris are below 100 μm^3. The average volume of the DLD-1 cell is 1553 μm^3, which is 5.25-fold larger than that of WBCs. Therefore, to minimize the volume overlap of DLD-1 cells and WBCs, the volume threshold criterion was set as 600 μm^3 and the proportion of DLD-1 cells below 600 μm^3 was 4.47%.

Figure S9B shows that the average amplitudes of WBCs and DLD-1 cells measured by impedance cytometry are 0.99 and 5.51 V, which indicates that the amplitude of DLD-1 cells is

DOI: 10.1021/acs.analchem.5b03147
Anal. Chem. 2015, 87, 10585−10592

5.57-fold larger than that of WBCs. The amplitude corresponding to a volume threshold criterion of 600 μm^3 is 2 V. Only 0.68% of WBCs exceed the amplitude of 2 V, and the proportion of DLD-1 cells below the amplitude criterion is 5%. These observations agree with the results obtained from the volume histogram based on the volume criterion of 600 μm^3. Therefore, an amplitude threshold of 2 V was set as one of the criteria for identifying DLD-1 cells from background normal blood cells.

Signal Processing Algorithm. An excitation signal, superposed by two sinusoidal signals of 500 kHz and 10 MHz, is applied to the excitation electrodes out of phase with one another. When a cell passes through one of the excitation and sensing electrode pairs, the imbalance between two electrode pairs induces an amplitude-modulated signal on the sensing electrode. To obtain the amplitude and phase for the two frequencies of bare DLD-1 cells, WBCs, GNP clot, and DLD-1 cells covered by GNPs, two lock-in amplifiers were used to process the signal generated on the sensing electrode, as shown in Figure S5. This signal processing produced four signals as X_{LF} (black) and Y_{LF} (red) signals for 500 kHz and X_{HF} (green) and Y_{HF} (blue) signals for 10 MHz, where the X and Y signals are the real and imaginary components of the output signals for each frequencies, respectively. The peak-to-peak values of X and Y signals were measured using a DAQ system and using the measured data, the amplitude and phase of the output signals were calculated using the LabVIEW software.

As shown in Figure S10, the X and Y signals of bare DLD-1 cells, WBCs, and DLD-1 cells covered by GNPs show a similar tendency, while those of GNP clot are different. Thus, GNP clot can be easily discriminated by the phase of the output signals. The peak-to-peak value of the X_{HF} (green) signal of bare DLD-1 cells is larger than that of the Y_{HF} (blue) signal, while the opposite was true in the case of DLD-1 cells covered by GNPs. Making use of this phenomenon, i.e., the phase difference of the 10 MHz output signal, the two populations can be distinguished. In addition, the X_{LF} (black) and Y_{LF} (red) signals of bare DLD-1 cells and DLD-1 cells covered by GNPs are much higher than those of WBCs, thereby allowing discrimination of DLD-1 cells and WBCs.

Scatter Plot of Amplitude versus Phase. Figure 4 shows a scatter plot of the amplitude at the low frequency of 500 kHz versus the phase at the high frequency of 10 MHz of bare DLD-1 cells (green dot), WBCs (black), and DLD-1 cells covered by GNPs (red), and the measurements were performed separately. The scatter plot for WBCs shows that most amplitudes were less than 2 V and the phases were between 0° and −40°, with an average of −21.2°. A few persistent RBCs and cell debris also appeared at lower than −40°. In the case of bare DLD-1 cells, the amplitudes were widely distributed due to the various size of DLD-1 cells, where the average was 5.51 V, as shown in Figure S9B. Whereas, the phases were mostly distributed between 0° and −40°, with an average of −21.24°. The experimental results indicate that bare DLD-1 cells and WBCs can be easily discriminated by the amplitude, but not by the phase.

After labeling of DLD-1 cells with MNBs and GNPs, the CTC-enrichment device was first used to enrich DLD-1 cells and remove free GNPs, which may cause discrimination errors in impedance cytometry. The scatter plot of DLD-1 cells covered by GNPs shows that the amplitudes were mostly between 2 and 8 V. Thus, the amplitude threshold criterion for

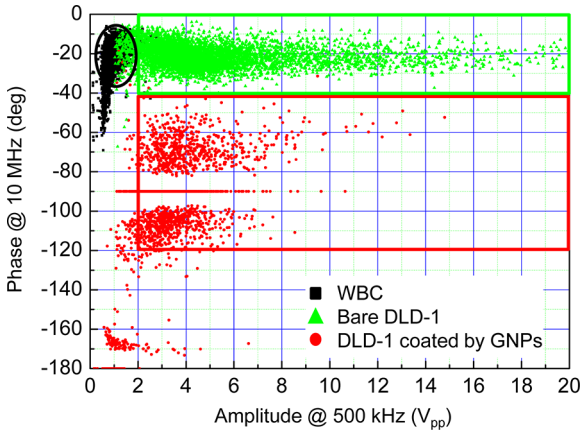

Figure 4. Scatter plot of amplitude at 500 kHz versus phase at 10 MHz of bare DLD-1 cells, WBCs, and DLD-1 cells covered by GNPs. The cell populations were measured separately. The amplitude criterion between DLD-1 cells and WBCs was set as 2 V. To identify DLD-1 cells covered by GNPs, the phase criterion was set between −40° and −120°.

distinguishing DLD-1 cells covered by GNPs and WBCs can be set as 2 V. The phase of DLD-1 cells covered by GNPs had a wide range between −40° and −120° due to the variation of GNP coverage rate on DLD-1 cells. The average phase of DLD-1 cells covered by GNPs was −87.72°, which is delayed by about 66.5° compared with the average phase of −21.24° for bare DLD-1 cells. Therefore, the phase criterion can be set between −40° and −120°. As shown in Figure 4, although the phase distribution seems to show two groups on both sides of −90°, this was caused by the voltage threshold level programmed to filter out the electrical noise of X and Y signals. The data below −120° are regarded as indicating persistent residual free GNPs, which are separated by the CTC-enrichment device due to their native magnetic properties or nonspecific binding with MNBs. Consequently, DLD-1 cells within the region of amplitude over 2 V and phase between −40° and −120° were about 94% of the total measured DLD-1 cells. This result demonstrated that the amplitude and phase criteria are acceptable for discriminating DLD-1 cells from normal blood cells.

Discrimination of DLD-1 Cells from Blood. To verify the feasibility of the CTC-eChip, 100−10 000 DLD-1 cells, stained with a membrane-permeable nucleic acid fluorescent dye (SYTO 13; Invitrogen), were spiked into 100 μL of peripheral blood. The blood samples were first treated using RBC lysis buffer. The RBC lysate was washed and resuspended in 100 μL of PBS. Then, anti-EpCAM antibodies, MNBs, and GNPs were added in sequence and incubated for 20 min at 4 °C. Finally, the samples were diluted with 100 μL of 0.1% BSA in PBS.

The average enrichment efficiency and fold enrichment of the device were 37% and 534-fold, as shown in Table 2. The number of DLD-1 cells separated by the CTC-enrichment device was measured by counting fluorescently stained DLD-1 cells flowing into outlet no. 1. The low enrichment efficiency was due to the sedimentation of DLD-1 cells covered by GNPs. As the mass density of GNPs is about 2 g cm^{-3}, DLD-1 cells covered by GNPs easily settle onto the floor of the sample injection syringe. Meanwhile, the proportion of DLD-1 cells flowing into outlet no. 1 among the total DLD-1 cells flowing into outlets no. 1 and no. 2 was about 98.15%. The observation indicated that the majority of DLD-1 cells injected into the

DOI: 10.1021/acs.analchem.5b03147
Anal. Chem. 2015, 87, 10585−10592

Table 2. Experimental Results of Enrichment and Electrical Discrimination

	CTC-enrichment device			impedance cytometry	
spiked number of DLD-1	separated number	enrichment efficiency (%)	fold	detected number	discrimination efficiency (%)
1030	319	31	300	306	96
516	258	50	560	241	94
425	187	44	560	173	93
280	115	41	690	99	86
96	20	21	560	18	90
avg.		37	534		94

microchannel of the CTC-enrichment device were separated into outlet no. 1. Thus, it is assumed that the enrichment efficiency can be markedly improved by use of an advanced sample injection system, such as a pressurized fluid pump. In addition, conductive nanoplates, with lower mass density and higher conductivity than GNPs used here, would avoid the sedimentation problem and increase the detection accuracy based on the phase difference. Besides, if the nanoplate is developed as a smart material having proper magnetic properties as well as conductivity, the sample preparation procedure can be simplified and performed more rapidly.

Figure 5A shows a scatter plot of amplitude at 500 kHz versus phase at 10 MHz for the case where the number of DLD-1 cells separated by the CTC-enrichment device was 319. The number of DLD-1 cells located within the range of the amplitude and phase criteria was 306. Data points less than 2 V and placed between −20° and −70° are regarded as WBCs. Due to the nonspecific binding of GNPs on WBCs, the average phase was measured as −48.2°, which was slightly shifted compared with the previous result of −21.2°. Figure 5B shows the results of regression analysis of the number of DLD-1 cells separated by the CTC-enrichment device versus the number detected by impedance cytometry. The number of DLD-1 cells detected was determined from the data points within the range of the amplitude and phase criteria. The detailed experimental results are summarized in Table 2. Consequently, the detection rate of DLD-1 cells was about 94% of the enriched DLD-1 cells, indicating that 94% of the enriched DLD-1 cells can be identified by impedance cytometry based on the amplitude and phase criteria.

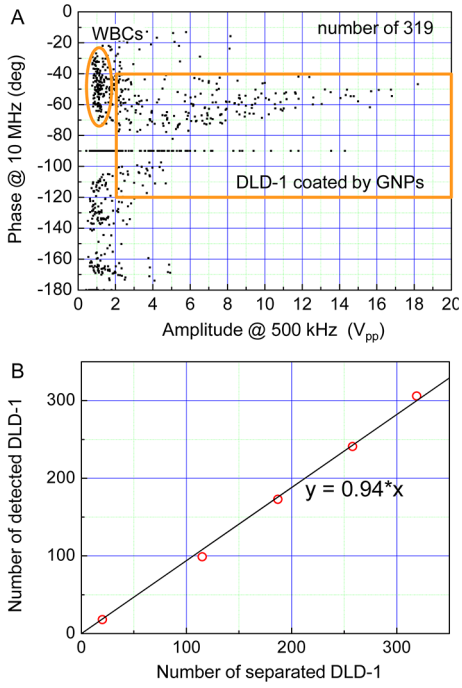

Figure 5. (A) Scatter plot of amplitude at 500 kHz versus phase at 10 MHz for the case where the number of DLD-1 cells separated by the CTC-enrichment device is 319. (B) Regression analysis for the detection efficiency of impedance cytometry with respect to the number of DLD-1 cells separated by the CTC-enrichment device.

Finally, to determine whether discriminated CTCs can be applied to downstream assays at the molecular levels, keratin 19 (KRT19) as an epithelial originated tumor-specific gene was measured by the RT-PCR method. Figure S11 shows that the tumor-specific gene can be detected from discriminated CTCs, thereby demonstrating that MNBs and GNPs as tagging materials used here do not affect subsequent downstream assays at the molecular level.

CONCLUSIONS

This study introduced the CTC-eChip, which can electrically distinguish CTCs from human peripheral blood based on lateral magnetophoresis and GNPs. The CTC-eChip was composed of a CTC-enrichment device and impedance cytometry as a two-step platform for separation and identification of CTCs. The enrichment process, based on lateral magnetophoresis and MNBs, increased the electrical discrimination accuracy of impedance cytometry by elimination of most normal blood cells and unwanted debris, which may create noise. Although sedimentation of DLD-1 cells covered by GNPs was problematic due to the high mass density of GNPs, the separation efficiency of DLD-1 cells injected into the CTC-enrichment device was 98.15%. From the result of the separation efficiency, we concluded that the coverage rate of GNPs does not disrupt binding of MNBs to DLD-1 cells. As a lot of GNPs are attached to DLD-1 cells, they might easily sink down due to the high mass density of GNP, thereby possibly decreasing the enrichment efficiency. GNPs as a highly conductive material induced a phase shift, thus reducing the impedance between the excitation and sensing electrodes. On the basis of the electrical properties of GNPs, impedance cytometry was used to accurately detect DLD-1 cells covered by GNPs from blood. As the CTC-eChip was implemented using only magnets and electrical processing circuitry without expensive, bulky equipment, it can be easily realized in microchip format. In addition, the discriminated CTCs can be applied to downstream assays at the cellular and molecular levels, because the tagging materials of MNBs and GNPs do not affect biological assays. Furthermore, as the proposed CTC-eChip does not require fluorescence labeling, the separated CTCs are also suitable for precise molecular analysis, such as next-generation sequencing.

ASSOCIATED CONTENT

Supporting Information

The Supporting Information is available free of charge on the ACS Publications website at DOI: 10.1021/acs.analchem.5b03147.

DOI: 10.1021/acs.analchem.5b03147
Anal. Chem. 2015, 87, 10585−10592

Experimental details, equivalent circuits, simulation results, Coulter Counter analysis, electrical signal graphs, and RT-PCR result. (PDF)

AUTHOR INFORMATION

Corresponding Author

*E-mail: mems@inje.ac.kr.

Author Contributions

The manuscript was written through contributions of all authors. All authors have given approval to the final version of the manuscript.

Notes

The authors declare no competing financial interest.

ACKNOWLEDGMENTS

This work (NRF-2012R1A2A2A03045174) was supported by the Midcareer Researcher Program through an NRF grant funded by the MEST.

REFERENCES

(1) Cristofanilli, M.; Budd, G. T.; Ellis, M. J.; Stopeck, A.; Matera, J.; Miller, M. C.; Reuben, J. M.; Doyle, G. V.; Allard, W. J.; Terstappen, L. W. M. M.; Hayes, D. F. *N. Engl. J. Med.* **2004**, *351*, 781−791.

(2) Pantel, K.; Brakenhoff, R. H.; Brandt, B. *Nat. Rev. Cancer* **2008**, *8*, 329−340.

(3) Riethdorf, S.; Fritsche, H.; Müller, V.; Rau, T.; Schindlbeck, C.; Rack, B.; Janni, W.; Coith, C.; Beck, K.; Jänicke, F.; Jackson, S.; Gornet, T.; Cristofanilli, M.; Pantel, K. *Clin. Cancer Res.* **2007**, *13*, 920−928.

(4) Miller, M. C.; Doyle, G. V.; Terstappen, L. M. M. *J. Oncol.* **2010**, *2010*, 617421.

(5) Allard, W. J.; Matera, J.; Miller, M. C.; Repollet, M.; Connelly, M. C.; Rao, C.; Tibbe, A. G. J.; Uhr, J. W.; Terstappen, L. W. M. M. *Clin. Cancer Res.* **2004**, *10*, 6897−6904.

(6) Racila, E.; Euhus, D.; Weiss, A. J.; Rao, C.; McConnell, J.; Terstappen, L. W. M. M.; Uhr, J. W. *Proc. Natl. Acad. Sci. U. S. A.* **1998**, *95*, 4589−4594.

(7) Gerhardt, T.; Woo, S.; Ma, H. *Lab Chip* **2011**, *11*, 2731−2737.

(8) Tan, S. J.; Lakshmi, R. L.; Chen, P.; Lim, W.-T.; Yobas, L.; Lim, C. T. *Biosens. Bioelectron.* **2010**, *26*, 1701−1705.

(9) McFaul, S. M.; Lin, B. K.; Ma, H. *Lab Chip* **2012**, *12*, 2369−2376.

(10) Lin, H. K.; Zheng, S.; Williams, A. J.; Balic, M.; Groshen, S.; Scher, H. I.; Fleisher, M.; Stadler, W.; Datar, R. H.; Tai, Y.-C.; Cote, R. J. *Clin. Cancer Res.* **2010**, *16*, 5011−5018.

(11) Zheng, S.; Lin, H. K.; Lu, B.; Williams, A.; Datar, R.; Cote, R. J.; Tai, Y.-C. *Biomed. Microdevices* **2011**, *13*, 203−213.

(12) Kim, M. S.; Sim, T. S.; Kim, Y. J.; Kim, S. S.; Jeong, H.; Park, J.-M.; Moon, H.-S.; Kim, S. I.; Gurel, O.; Lee, S. S.; Lee, J.-G.; Park, J. C. *Lab Chip* **2012**, *12*, 2874−2880.

(13) Sun, W.; Jia, C.; Huang, T.; Sheng, W.; Li, G.; Zhang, H.; Jing, F.; Jin, Q.; Zhao, J.; Li, G.; Zhang, Z. *PLoS One* **2013**, *8*, e75865.

(14) Park, J.-M.; Lee, J.-Y.; Lee, J.-G.; Jeong, H.; Oh, J.-M.; Kim, Y. J.; Park, D.; Kim, M. S.; Lee, H. J.; Oh, J. H.; Lee, S. S.; Lee, W.-Y.; Huh, N. *Anal. Chem.* **2012**, *84*, 7400−7407.

(15) Rosenberg, R.; Gertler, R.; Friederichs, J.; Fuehrer, K.; Dahm, M.; Phelps, R.; Thorban, S.; Nekarda, H.; Siewert, J. R. *Cytometry* **2002**, *49*, 150−158.

(16) Kim, S.; Han, S.-I.; Park, M.-J.; Jeon, C.-W.; Joo, Y.-D.; Choi, I.-H.; Han, K.-H. *Anal. Chem.* **2013**, *85*, 2779−2786.

(17) Chen, C.-L.; Chen, K.-C.; Pan, Y.-C.; Lee, T.-P.; Hsiung, L.-C.; Lin, C.-M.; Chen, C.-Y.; Lin, C.-H.; Chiang, B.-L.; Wo, A. M. *Lab Chip* **2011**, *11*, 474−483.

(18) Hoshino, K.; Huang, Y.-Y.; Lane, N.; Huebschman, M.; Uhr, J. W.; Frenkel, E. P.; Zhang, X. *Lab Chip* **2011**, *11*, 3449−3457.

(19) Nagrath, S.; Sequist, L. V.; Maheswaran, S.; Bell, D. W.; Irimia, D.; Ulkus, L.; Smith, M. R.; Kwak, E. L.; Digumarthy, S.; Muzikansky, A.; Ryan, P.; Balis, U. J.; Tompkins, R. G.; Haber, D. A.; Toner, M. *Nature* **2007**, *450*, 1235−1239.

(20) Karabacak, N. M.; Spuhler, P. S.; Fachin, F.; Lim, E. J.; Pai, V.; Ozkumur, E.; Martel, J. M.; Kojic, N.; Smith, K.; Chen, P.-i.; Yang, J.; Hwang, H.; Morgan, B.; Trautwein, J.; Barber, T. A.; Stott, S. L.; Maheswaran, S.; Kapur, R.; Haber, D. A.; Toner, M. *Nat. Protoc.* **2014**, *9*, 694−710.

(21) Mikolajczyk, S. D.; Millar, L. S.; Tsinberg, P.; Coutts, S. M.; Zomorrodi, M.; Pham, T.; Bischoff, F. Z.; Pircher, T. J. *J. Oncol.* **2011**, *2011*, 252361.

(22) Stott, S. L.; Hsu, C.-H.; Tsukrov, D. I.; Yu, M.; Miyamoto, D. T.; Waltman, B. A.; Rothenberg, S. M.; Shah, A. M.; Smas, M. E.; Korir, G. K.; Frederick, P.; Floyd, J.; Gilman, A. J.; Lord, J. B.; Winokur, D.; Springer, S.; Irimia, D.; Nagrath, S.; Sequist, L. V.; Lee, R. J.; Isselbacher, K. J.; Maheswaran, S.; Haber, D. A.; Toner, M. *Proc. Natl. Acad. Sci. U. S. A.* **2010**, *107*, 18392−18397.

(23) Hur, S. C.; Mach, A. J.; Di Carlo, D. *Biomicrofluidics* **2011**, *5*, 022206.

(24) Hou, H. W.; Warkiani, M. E.; Khoo, B. L.; Li, Z. R.; Soo, R. A.; Tan, D. S.-W.; Lim, W.-T.; Han, J.; Bhagat, A. A. S.; Lim, C. T. *Sci. Rep.* **2013**, *3*, 1259.

(25) Gupta, V.; Jafferji, I.; Garza, M.; Melnikova, V. O.; Hasegawa, D. K.; Pethig, R.; Davis, D. W. *Biomicrofluidics* **2012**, *6*, 024133.

(26) Fabbri, F.; Carloni, S.; Zoli, W.; Ulivi, P.; Gallerani, G.; Fici, P.; Chiadini, E.; Passardi, A.; Frassineti, G. L.; Ragazzini, A.; Amadori, D. *Cancer Lett.* **2013**, *335*, 225−231.

(27) Allan, A. L.; Vantyghem, S. A.; Tuck, A. B.; Chambers, A. F.; Chin-Yee, I. H.; Keeney, M. *Cytometry, Part A* **2005**, *65A*, 4−14.

(28) Cruz, I.; Ciudad, J.; Cruz, J. J.; Ramos, M.; Gómez-Alonso, A.; Adansa, J. C.; Rodríguez, C.; Orfao, A. *Am. J. Clin. Pathol.* **2005**, *123*, 66−74.

(29) Harouaka, R. A.; Nisic, M.; Zheng, S.-Y. *Journal of Laboratory Automation* **2013**, *18*, 455−468.

(30) Coumans, F. A. W.; van Dalum, G.; Beck, M.; Terstappen, L. W. M. M. *PLoS One* **2013**, *8*, e61770.

(31) De Giorgi, V.; Pinzani, P.; Salvianti, F.; Panelos, J.; Paglierani, M.; Janowska, A.; Grazzini, M.; Wechsler, J.; Orlando, C.; Santucci, M.; Lotti, T.; Pazzagli, M.; Massi, D. *J. Invest. Dermatol.* **2010**, *130*, 2440−2447.

(32) Asghar, W.; Wan, Y.; Ilyas, A.; Bachoo, R.; Kim, Y.-t.; Iqbal, S. M. *Lab Chip* **2012**, *12*, 2345−2352.

(33) Joo, S.; Kim, K. H.; Kim, H. C.; Chung, T. D. *Biosens. Bioelectron.* **2010**, *25*, 1509−1515.

(34) Spencer, D.; Elliott, G.; Morgan, H. *Lab Chip* **2014**, *14*, 3064−3073.

(35) Choi, H.; Kim, K. B.; Jeon, C. S.; Hwang, I.; Lee, S.; Kim, H. K.; Kim, H. C.; Chung, T. D. *Lab Chip* **2013**, *13*, 970−977.

(36) Lee, H.; Jung, J.; Han, S.-I.; Han, K.-H. *Lab Chip* **2010**, *10*, 2764−2770.

(37) Han, K.-H.; Frazier, A. B. *Lab Chip* **2006**, *6*, 265−273.

(38) Han, K.-H.; Frazier, A. B. *J. Appl. Phys.* **2004**, *96*, 5797−5802.

(39) Han, S.-I.; Joo, Y.-D.; Han, K.-H. *Sens. Actuators, B* **2012**, *171−172*, 1312−1320.

(40) Holmes, D.; Pettigrew, D.; Reccius, C. H.; Gwyer, J. D.; van Berkel, C.; Holloway, J.; Davies, D. E.; Morgan, H. *Lab Chip* **2009**, *9*, 2881−2889.

(41) Morgan, H.; Sun, T.; Holmes, D.; Gawad, S.; Green, N. G. *J. Phys. D: Appl. Phys.* **2007**, *40*, 61−70.

(42) Sun, T.; Gawad, S.; Green, N. G.; Morgan, H. *J. Phys. D: Appl. Phys.* **2007**, *40*, 1−8.

(43) Sun, T.; Bernabini, C.; Morgan, H. *Langmuir* **2010**, *26*, 3821−3828.

(44) Morgan, H.; Green, N. G. *AC Electrokinetics: Colloid and Nanoparticles*; Research Studies Press Ltd.: Hertfordshire, England, 2003.

(45) Grabowska, I.; Stachyra, A.; Góra-Sochacka, A.; Sirko, A.; Olejniczak, A. B.; Leśnikowski, Z. J.; Radecki, J.; Radecka, H. *Biosens. Bioelectron.* **2014**, *51*, 170−176.

DOI: 10.1021/acs.analchem.5b03147
Anal. Chem. 2015, 87, 10585−10592

(46) Nwankire, C. E.; Venkatanarayanan, A.; Glennon, T.; Keyes, T. E.; Forster, R. J.; Ducrée, J. *Biosens. Bioelectron.* **2015**, *68*, 382−389.
(47) Wu, Y.; Xue, P.; Kang, Y.; Hui, K. M. *Anal. Chem.* **2013**, *85*, 3166−3173.
(48) Recktenwald, D. *Cell separation methods and applications*; CRC Press: Boca Raton, FL, 1997.
(49) Lin, M. X.; Hyun, K.-A.; Moon, H.-S.; Sim, T. S.; Lee, J.-G.; Park, J. C.; Lee, S. S.; Jung, H.-I. *Biosens. Bioelectron.* **2013**, *40*, 63−67.
(50) Milner, B.; Penny, C.; Gibbon, V.; Kay, P.; Ruff, P. *J. Tissue Sci. Eng.* **2015**, *6*, 143.
(51) Han, S.-I.; Joo, Y.-D.; Han, K.-H. *Analyst* **2013**, *138*, 1529−1537.
(52) Yang, J.; Huang, Y.; Wang, X.; Wang, X.-B.; Becker, F. F.; Gascoyne, P. R. C. *Biophys. J.* **1999**, *76*, 3307−3314.
(53) Hoffman, R. A.; Britt, W. B. *J. Histochem. Cytochem.* **1979**, *27*, 234−240.
(54) Qiao, G.; Wang, W.; Duan, W.; Zheng, F.; Sinclair, A. J.; Chatwin, C. R. *IEEE Trans. Biomed. Eng.* **2012**, *59*, 2321−2329.
(55) Zhao, Y.; Zhao, X. T.; Chen, D. Y.; Luo, Y. N.; Jiang, M.; Wei, C.; Long, R.; Yue, W. T.; Wang, J. B.; Chen, J. *Biosens. Bioelectron.* **2014**, *57*, 245−253.

DOI: 10.1021/acs.analchem.5b03147
Anal. Chem. 2015, 87, 10585−10592